Classification of Adolescent Major Depressive Disorder via Static and Dynamic Connectivity

Bhaskar Sen, *Student Member, IEEE*; Kathryn R. Cullen; and Keshab K. Parhi, *Fellow, IEEE*

***Abstract*— This paper introduces an approach for classifying adolescents suffering from MDD using resting-state fMRI. Accurate diagnosis of MDD involves interviews with adolescent patients and their parents, symptom rating scales based on Diagnostic and Statistical Manual of Mental Disorders (DSM), behavioral observation as well as the experience of a clinician. Discovering predictive biomarkers for diagnosing MDD patients using functional magnetic resonance imaging (fMRI) scans can assist the clinicians in their diagnostic assessments. This paper investigates various static and dynamic connectivity measures extracted from resting-state fMRI for assisting with MDD diagnosis. First, absolute Pearson correlation matrices from 85 brain regions are computed and they are used to calculate static features for predicting MDD. A predictive sub-network extracted using *sub-graph* entropy classifies adolescent MDD *vs.* typical healthy controls with high accuracy, sensitivity and specificity. Next, approaches utilizing dynamic connectivity are employed to extract tensor based, independent component based and principal component based subject specific attributes. Finally, features from static and dynamic approaches are combined to create a feature vector for classification. A leave-one-out cross-validation method is used for the final predictor performance. Out of 49 adolescents with MDD and 33 matched healthy controls, a support vector machine (SVM) classifier using a radial basis function (RBF) kernel using *differential sub-graph* entropy combined with dynamic connectivity features classifies MDD *vs.* healthy controls with an accuracy of 0.82 for leave-one-out cross-validation. This classifier has specificity and sensitivity of 0.79 and 0.84, respectively.**

***Index Terms*— Major depressive disorder (MDD), *sub-graph* entropy, brain network, static functional connectivity, dynamic functional connectivity, resting-state, fMRI, classification, psychiatry, adolescent MDD**

I. Introduction

Major-depressive disorder (MDD) is a debilitating neuropsychiatric illness that impacts all aspects of patients' lives. This disorder is characterized by the presence of at least five of nine symptoms (low mood, lack of enjoyment, low energy, impaired sleep, impaired appetite, concentration difficulties, poor self-esteem, and suicidal thoughts) that cause impairment for at least two weeks. It impacts about 322 million people's lives worldwide [1]. Depression is prevalent in a large proportion of general population; however, for patients suffering from MDD, the symptoms of depression are very persistent and critical. Although MDD is a serious life threatening psychiatric disease, the neurobiology underlying MDD is still poorly understood. Advancing this knowledge is needed to guide diagnosis and treatment strategies, with the goal of restoring healthy brain development and preventing negative outcomes such as suicide and functional impairment over the lifespan. Among the different age groups of population vulnerable to MDD, adolescents constitute a major subgroup. The current diagnostic process for adolescent MDD involves a subjective understanding of the patient which includes behavioral examinations, symptom ratings and interviews with parents [2]. An artificial intelligence (AI) assisted clinical diagnostic tool based on functional magnetic resonance imaging has the potential to assist a clinician to diagnose MDD directly using brain scans [3].

The current study applied several novel analytic tools to resting-state fMRI data from adolescents with and without MDD. Specifically, we (1) examined correlation between pairs of brain regions, (2) calculated graph-theoretic properties of functional networks, and (3) measured dynamic connectivity properties of these networks. This paper develops a machine learning based diagnostic tool (classifier) combining graph-theoretic and dynamic connectivity properties to discriminate and identify adolescents suffering from MDD from typical healthy developing adolescents. The classifier learns prediction rules based on resting-state functional magnetic resonance imaging (fMRI) based attributes of subjects. Identifying patient-specific features for classifying adolescent MDD is a very important step, as if left without proper treatment, the subjects may have atypical neuronal development. However, how the resting-state brain functional network changes among adolescents with MDD remains unknown. Thus finding specific markers associated with MDD is of significant interest.

Concurrent fMRI based psychiatric research has shown that fMRI can be used to diagnose different neuronal disorders [4]–[7]. Functional magnetic resonance imaging provides an in-vivo measurement of brain activity during resting-state (rs-fMRI) or task (t-fMRI). Specifically, fMRI measures the change of blood-oxygen level dependent (BOLD) signal, when a person is scanned. This produces a 4-D activation image of brain function, where the first three dimensions show the *spatial* brain structure and the fourth dimension shows the change of activation over time [6], [8]. The time component of fMRI scans can be utilized to extract correlation based functional connectivity of brain regions. When a person is awake in rest condition, some regions in the brain are always activated (default mode network). For rs-fMRI, the spontaneous regional interaction between brain regions are measured. Resting-state fMRI signal have been hypothesized to be meaningful for identifying psychiatric patients as the hemodynamic response is not confounded by any task response [9]. The current paper considers only the analysis of rs-fMRI for adolescent MDD patients and typically developing adolescents.

The goal of this paper is to classify adolescent MDD patients from healthy controls accurately. In this process, we extract a brain sub-network from rs-fMRI that has good classification performance for identifying adolescent MDD *vs.* healthy controls. We use absolute correlation coefficients, graph-theoretic properties of functional network, and dynamic connectivity properties of human brain for classifying MDD and healthy controls. First we use absolute correlation and network based features for predicting MDD. Second, network measures using *sub-graph* entropy [10] and specifically differential node entropy and edge entropy are used to extract most important regions and edges impacted in adolescent MDD. Edge entropy is then used to extract a sub-network containing 105 edges. The static connectivity measures by itself achieve high classification performance.

Manuscript received July 24, 2020; revised November 12, 2020; accepted December 1, 2020. This research was supported in part by the National Science Foundation by grant number CCF-1954749.

Bhaskar Sen and Keshab K. Parhi are with Department of Electrical and Computer Engineering, University of Minnesota, Minneapolis (e-mail: parhi@umn.edu), Kathryn R. Cullen is with Department of Psychiatry and Behavioral Sciences, University of Minnesota, Minneapolis

Following this, a dynamic functional connectivity feature extraction technique based on constrained parallel factor analysis (PARAFAC) tensor decomposition is carried out. The dFC features achieves high sensitivity. Finally, a *joint* connectivity approach combining features from static and dynamic connections leads to a high classification accuracy, sensitivity and specificity for classification of MDD *vs.* healthy.

A. Related Work

Recent advancements in machine learning in neuroimaging has unraveled the relationship between computer aided designs and psychiatry. Furthermore, advances in complex network theory, blind source separation have also permeated neuroimaging and psychiatry. In a complex network, different measures can be used to find the important nodes [10], [11]. These metrics denote the cohesiveness or segregation among different nodes. Network segregation refers to the *local* characteristics at each node, *i.e.*, how a particular node is affected by the interaction with its neighbors. Network integration refers to the large-scale behavior of the whole graph (*global* characteristics). In particular, *local efficiency (LE)* [12], [13], *clustering coefficient (CE)* [14] and *betweenness centrality (BC)* [15] measures are examples of local network segregation. Global integration can be specified in terms of *global efficiency (GE)* [12] and *modularity* [16]. An important network metric defines important nodes to be those having the highest number of neighbors. This *metric* is known as degree centrality [17].

A more complex *metric* using *information-theoretic* network measures [18] was used in [19] to extract leaders and followers from a directed communication network. Mackenzie [18] showed that *information-theoretic* importance can be used as centrality in a communication network. An *information-theoretic* network segregation *metric*, referred as *sub-graph* entropy [10], has been shown to be useful for classifying brain *states*. This network metrics was used in [6] for diagnosing adolescent obsessive compulsive disorder. *Sub-graph* entropy is calculated using Shannon's entropy function over normalized edge weights. *sub-graph* entropy is *larger* for those cases where the edge weights within a sub-network are *uniform*. Typically, *dominance* of edge strength between two regions *reduces* the *sub-graph* entropy. An example of calculation of graph entropy, *sub-graph* entropy, node and edge entropy is illustrated in Fig. S1 in Supplementary Information (SI). The reader is referred to [6], [10] for more details.

Some of the above measures were used previously for comparing characteristics between two groups (*e.g.*, schizophrenia *vs.* healthy [4], [20], Alzheimer's disorder *vs.* healthy [21], [22], borderline personality disorder *vs.* healthy [5], and obsessive compulsive disorder *vs.* healthy [6], [23]). Hypothesis driven association studies can extract statistically significant functional neural correlates for psychiatric disorder. In the current paper, we propose a combined static and dynamic connectivity approach to predict whether an adolescent has MDD. Using tools from communication and network information theory and tensor analysis, we show that a network measure called *sub-graph* entropy (node and edge entropy) introduced in our recent paper [10] and constrained parallel factor analysis [8], [24] can perform this task with high accuracy. Additionally, node and edge entropy were used to rank brain regions and edges, respectively. The important predictive sub-network extracted in this process carries information regarding the possible neuronal impairment during MDD.

B. Contributions

The contributions of this paper are summarized as follows.

- Utilizing a number of static connectivity measures, *e.g.*, absolute correlation coefficient values, network metrics and *sub-graph* entropy, the paper demonstrates that static connectivity measures alone have high accuracy for classifying adolescent MDD *vs.* healthy controls.
- The paper also shows the utility of dynamic connectivity profiles for identifying adolescent MDD. Dynamic components extracted using constrained-PARAFAC and ICA achieve high sensitivity but low specificity for classification of MDD. This observation indicates that dFC metrics alone may not be able to diagnose MDD accurately.
- A joint static and dynamic feature concatenation process is proposed for accurate classification of MDD using rs-fMRI data. This feature combination process improves the leave-one-out classification accuracy for classifying MDD *vs.* healthy controls by 3% compared to previously known baseline methods [25].
- Finally, the regions and functional edges extracted by predictive *sub-graph* are then compared with the previous literature. We show that the predictive sub-network contains regions that belong to well-known large-scale brain networks that are traditionally implicated in adolescent MDD.

TABLE I: Demographic and clinical score information for the subjects

Demographic Information	Healthy	MDD	$p-value$
# of samples (n)	33	49	-
Biological sex (Male/ Female)	8/24	13/36	0.88
Age – mean (SD)	15.63 (2.05)	15.62 (2.86)	0.9
Clinical Severity	Healthy	MDD	$p-value$
CDRS-R [26] (T scores) - mean (SD)	NA	77 (6)	NA
BDI-II [27] (most severe) - mean (SD)	3(4)	29(13)	< 0.001

II. Materials and Methods

A. Dataset and Preprocessing

The data collection process and experiments mentioned in the present work that include human subjects were approved by the University of Minnesota *Institutional Review Board* (IRB) (Study number 0804S30542, approval date 9/16/2015). The study consisted of 49 adolescents with MDD and 33 healthy control subjects. The subjects were similar with respect to age, sex, or handedness as described in [25], [28]. The two groups had significantly different values for CDRS-R [26] scores and BDI-II [27] scores. Additionally, there were no statistically significant differences in scores at the group level for MDD patients on medication and no-medication. We describe the data acquisition and pre-processing steps following [25], [28]. A table containing the demographic and clinical information is shown in Table I.

The study involved only adolescent subjects (12-19 years). Resting-state functional magnetic resonance images were captured for 6 minutes with the following parameter specifications: repetition time (TR) = 2s, field of view (FOV) = 220×220mm, and voxel size of $3.43 \times 3.43 \times 4$ mm. There were 34 interleaved slices with no skip. During the scanning process, adolescents undergoing the study were awake. They were advised to close their eyes, relax and they were asked not to think about something specific.

Following rs-fMRI data acquisition, FMRIB Software Library (FSL) [29] tools were used to preprocess the raw voxel time-series. This step involves removing skulls from images, correcting any distortions, correcting motion that may distort images. Finally, the images were registered to $2 \times 2 \times 2$ mm Montreal Neurological Institute space (**MNI**). In order to remove many physiological artifacts (e.g., heart rate, respiration signal and linear trend), we used RETROICOR process as described in [30]. Additionally, FreeSurfer [31] produced white matter and cerebrospinal fluid were aligned with rs-fMRI utilizing FLIRT program available through FSL [29]. More details of the preprocessing can be found in [28]. After the preprocessing step, the Desikan atlas [32] was used to extract mean time-series from 85 cortical and sub-cortical regions. The regions are given

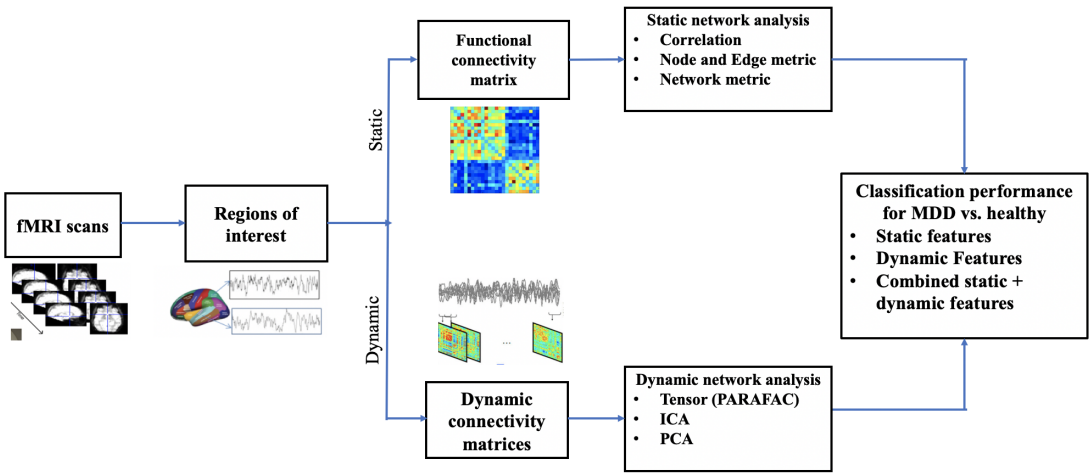

Fig. 1: MDD classification pipeline using static and dynamic features. Functional MRI scans are used to extract static and dynamic features that are later used for leave-one-out classification process.

in [32] and also in Supplementary Information (Table A1). The extracted mean time-series from each subject were then subjected to wavelet frequency decomposition into 4 frequency bands using a db-4 wavelet [5]. The time-series corresponding to the previous frequency bands are described as: B1 ($0.015 \sim 0.03$ Hz), B2 ($0.03 \sim 0.06$Hz), B3 ($0.06 \sim 0.12$ Hz), B4 ($0.12 \sim 0.25$ Hz) as described in [25]. A pipeline demonstrating the whole experimental process is shown in Fig. 1.

B. Static Features

1) Correlation Features: A number of connectivity measures have been described in literature [33] to estimate human brain functional connectivity. In this paper, we use Pearson's correlation coefficient as the metric for representing functional connectivity. Pearson correlation coefficient was calculated for every frequency band ($B1...B4$) using the formulae given below:

$$P^f_{i,j} = P^f_{j,i} = \frac{E[(r^f_i - \hat{r}^f_i)(r^f_j - \hat{r}^f_j)]}{\sqrt{E[(r^f_i - \hat{r}^f_i)^2]}\sqrt{E[(r^f_j - \hat{r}^f_j)^2]}} \quad (1)$$

.

Here $\hat{r}^f_i$ is the average of time-series for frequency band f and the region id is denoted by i. Here four adjacency matrices are created for every pair of brain regions for each subject. In this view, each of these matrices may represent adjacency matrices in functional graph where each entry represents an edge. Absolute value of these correlation coefficients are used for further processing. Thus the number of features for each frequency band is $\frac{85\times84}{2} = 3570$. These unique correlation values are later used as features for the classification task.

2) Network Features: As mentioned before, from each subject, four 85×85 adjacency matrices [25] were extracted. The adjacency matrices contain absolute Pearson's correlation coefficients. From these adjacency matrices, we calculated network integration and segregation measures that describe each subject's functional brain network structure using *Brain Connectivity Toolbox* (BCT) [1]. Each of the adjacency matrices are then binarized keeping $\{5\%,\ 20\%,\ 35\%,\ 50\%\}$ of the highest values. Thus at each frequency band, every subject has the same number of edges at each sparsity level.

We describe the network feature extraction process following [25] as we use them as baseline features in this paper. On a local node level in the network, three features namely *local efficiency (LE), clustering coefficient (CC)* and *betweenness centrality (BC)* were computed [5], [34]. At a global level, we calculated two features namely, *modularity* and *global efficiency* [34]. The local and global features in the network represent complementary viewpoint of the network for segregation and integration of nodes, respectively. Hence from each subject, we extract $85 \times 3 \times 4$ (for 3 features at each node) $+4 \times 2$ (for *modularity and global efficiency*)= 1028 network features corresponding to the frequency bands.

An overview of the network based features is mentioned next following the descriptions in [25]. *Local efficiency* is computed using the summation of inverse of the shortest paths to the neighbors of a node. This metric is used to understand how efficient a node is for transferring information between two neighboring nodes. *Clustering coefficient* is calculated by the number of triangles created around a node out of all possible triangles. *Betweenness centrality* of a node is calculated as the percentage of shortest paths that contain the node. *Modularity* metric measures how a network is sub-divided into smaller dense sub-networks with sparse inter-connections. *Global efficiency* describes the efficiency of information transfer within the whole graph. These network measures were also previously used for classifying MDD *vs.* healthy from fMRI data as described in [25]. More details of the network measures can be found in [14].

3) Sub-Graph Entropy: We have recently shown that *sub-graph* entropy can effectively classify brain *states* for task *vs.* no-task [10] and healthy *vs.* psychiatric patients [6]. *Sub-graphs* can denote any portion or sub-structure of the main graph. For a *sub-graph* $G_s = (V_s, E_s)$, of main graph $G = (V, E)$, the *sub-graph* entropy can be computed as follows:

$$H\left(G_s\right) = -\sum_{x,x' \in V_s} q(x,x') \log\left(q(x,x')\right)$$

where $q(x,x')$ denotes the normalized edge weight between nodes (x,x') for *sub-graph* G_s. For calculating the node entropy of node x, only the *sub-graph* containing the 1-hop neighborhood of node x is used. Here logarithm is computed with respect to base 2. Usefulness of graph entropy as a centrality measure has been demonstrated in [18], [19] and extended to *sub-graph* entropy in [10]. Note that, *sub-graph* entropy is *larger* for those cases where the edge weights within a sub-network are *uniform*. Typically, *dominance* of edge strength between two regions *reduces* the *sub-graph* entropy.

Node Entropy: Node entropy [10] refers to a *sub-graph* entropy of structure containing a graph node and its immediate neighbors. Although 1-hop neighborhood has been generally used to define node substructure, k-hop neighborhood may also be considered. In this paper, we only consider well understood 1-hop neighborhood

[1] https://sites.google.com/site/bctnet/

structure to calculate node entropy. Thus only the edges in the immediate neighborhood of a node are extracted. The node entropy values are used separately as features for classification.

Edge Entropy: Edge entropy [10] refers to a *sub-graph* entropy of structure containing an edge and the immediate neighbors of nodes that the edge connects. In this paper, we only consider well understood 1-hop neighborhood structure of an edge to calculate edge entropy. Thus only the edges in the immediate neighborhood of the two nodes of an edge are extracted for the calculation. The edge entropy values are used separately as features for classification. Illustrative examples of calculating graph entropy, *sub-graph* entropy for individual graph and a group of networks are described in [10].

Differential *Sub-Graph* (Node and Edge) Entropy:

Differential (node/edge) entropy refers to difference in node or edge entropy values when the same graph is analysed for two different conditions. Thus when a subject suffers through a mental disorder, it is hypothesized that a healthy functional connectivity structure is disrupted and thus the segregation/integration pattern of nodes/edges change [10]. The nodes/edges that undergo most change in local structural pattern can be extracted based on the highest change in the *sub-graph* entropy. Thus a change of a relative distribution of edge values for each subject is captured. A brief description for differential node entropy is given next. Assume there are two groups G^1 and G^2 (in the current scenario, they refer to healthy and MDD, respectively). The node entropy for node v_i for G^1 and G^2 are denoted as $H(G^1_{v_i})$ and $H(G^2_{v_i})$, respectively. Then differential node entropy is calculated as $|H(G^1_{v_i}) - H(G^2_{v_i})|$ [10]. The regions having higher differential node entropy are thought to have undergone the most functional connectivity changes. The same calculation process for extracting edges that have undergone disruption for MDD is carried out as well. In the next section, we describe how a leave-one-out classification process is able to extract a sub-network containing important edges predictive of MDD.

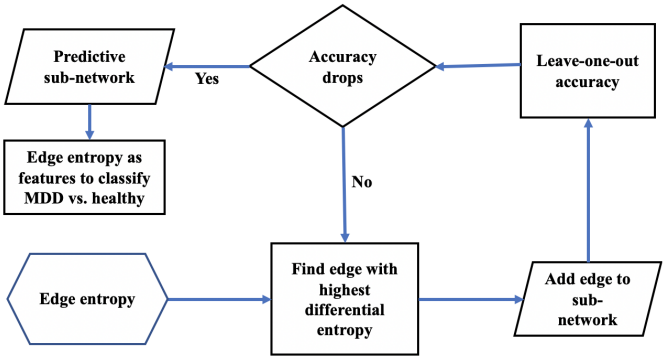

Fig. 2: Leave-one-out process for identifying a predictive sub-network that can classify MDD *vs.* healthy.

4) Extracting Predictive Sub-Network Based on Edge Entropy: As mentioned earlier, the edge entropy values were used to classify two groups (healthy *vs.* MDD). In order to extract a *sub-graph* associated with the disruption of functional network during MDD, we used a leave-one-out analysis based on classification accuracy [6], [35]. This edge selection framework involves finding top ranked edges at each iteration and add it to the sub-network. Then the leave-one-out accuracy of the edge entropy values (that belong to only the sub-network) is measured. We stop adding edges to the sub-network once the accuracy drops beyond certain number of edges. This process is illustrated in Fig. 2. Leave-one-out classification scheme is a commonly used classification scheme for mitigating the overfitting effect due to small sample size and high number of features [20]. In all iterations, the classifier used is support vector machine with radial basis kernel. The ranking process is also carried out in a leave-one-out manner, where it is performed 82 times. At each time, the ranking of regions/edges is carried out keeping one out and then a histogram demonstrating the stability of ranking process is plotted. In order to compare the predictive performance with other sub-networks, *union* and *intersection* of top regions and edges are employed for classification [10]

C. Dynamic Features

Dynamic functional connectivity (dFC) refers to brain network that changes over time. Dynamic connectivity is usually extracted using sliding-window Pearson's correlation matrices extracted from fMRI time-series containing regions of interest (85 regions). The collection of symmetric correlation matrices for each subject are then vectorized and stacked along the time dimension to create the dFC matrix for that subject. Note in this case, ($dim1$ = edges, $dim2$ = temporal) for every subject. Features were extracted from these dFC matrices using the methods below. We briefly describe the dynamic features following the description in [24].

1) Tensor Component Analysis: Tensor components analysis has recently been introduced for extracting dFC features [38]. Tensor decomposition makes use of high-dimensional blind source separation techniques to create common edge maps and temporal profiles across subjects. Also it produces subject-wise variations of those spatio-temporal components. We have recently introduced constrained-PARAFAC for predicting different phenotypes from fMRI data [24]. PARAFAC decomposition has better uniqueness properties and interpretability [39] in comparison with matrix decomposition. The scans from a group of subjects were concatenated to form a 3-way tensor where the $dim3$ = subject. We denote the 3-way tensor of size $I_1 \times I_2 \times I_3$ as $\mathcal{X}_{I_1,I_2,I_3}$. The constrained-PARAFAC decomposition is stated as:

$$\min_{\tilde{\mathcal{X}}} ||\mathcal{X} - \tilde{\mathcal{X}}||_F^2 \; s.t. \; \tilde{\mathcal{X}} = (A, B, C), A^T A = I, \; C \geq 0$$

2) Principal Component Analysis (PCA): [37]: Principal Component Analysis projects the dynamic functional connectivity matrices extracted from each subject into a common subspace (principal components). PCA analysis was performed on the collection of sliding-window correlation vectors stacked for all subjects. The scans from a group of subjects were concatenated in time dimension to create a long matrix of size $I_1 \times I_2 I_3$. This process extracted subject-wise unique time-series for each common principal component. The means of the time-series were chosen as features for prediction.

3) Independent Component Analysis (ICA): [36]: Similar to PCA, Independent Component Analysis projects the dynamic functional connectivity matrices extracted from each subject into a common subspace (termed as independent components). ICA has received widespread popularity in dFC analysis from fMRI. To extract ICA features, the scans from a group of subjects were concatenated in time dimension to create a long matrix of size $I_1 \times I_2 I_3$. ICA extracts common dFC space that are statistically independent to each other. Also this process finds out unique time-series for each of the components for subjects. The means of the time-series were chosen as features for prediction.

For Constrained-PARAFAC, PCA and ICA, the number of components required for the analysis was fixed based on cross-validation accuracy. In all blind source separation methods, source separations were done on the training set and the leave-one-subject out case was projected on the sources for extracting the features. Particularly for PCA, the number of optimal components were chosen based upon in-fold validation accuracy. As a result, each fold had its own PCA variance associated with it. The minimum variance captured was 92% and maximum variance captured was 99%.

TABLE II: Leave-one-out classification results for various feature sets and their combinations. The number of features shown in the table is the number that had maximum occurrence during the leave-one-out validation.

Types of features	Methods	# of Features	Accuracy	Sensitivity	Specificity	Classifier
Static features	Correlation [25]	10	0.74	0.82	0.64	SVM RBF
	Network features [25]	10	0.67	0.84	0.42	SVM RBF
	Correlation + Network features [25]	20	0.79	0.86	0.70	SVM RBF
	Node entropy [10]	25	0.67	0.84	0.42	SVM RBF
	Predictive sub-network [6]	105	0.80	0.84	0.76	SVM RBF
	Union *sub-graph* entropy [6]	130	0.80	0.84	0.76	SVM RBF
	Intersection *sub-graph* entropy [6]	95	0.77	0.82	0.7	SVM RBF
Dynamic features	Constrained-PARAFAC [24]	20	0.61	**0.96**	0.15	SVM RBF
	ICA [36]	20	0.62	0.92	0.18	RF # of T 10
	PCA [37]	20	0.57	0.86	0.15	RF # of T 10
Combined features (*proposed*)	Predictive sub-network + Constrained-PARAFAC	125	**0.82**	0.84	**0.79**	SVM RBF
	Predictive sub-network + Correlation + Network features	125	0.78	0.87	0.64	SVM RBF
	Predictive sub-network + Correlation	115	0.79	0.90	0.64	SVM RBF
	Predictive sub-network + Network features	115	0.80	0.94	0.61	SVM RBF
	Constrained-PARAFAC + Correlation + Network features	40	0.65	0.84	0.36	SVM RBF
	Constrained-PARAFAC + Correlation	30	0.67	0.84	0.42	SVM RBF
	Constrained-PARAFAC + Network features	30	0.65	0.84	0.36	SVM RBF

D. Combination of Features

We hypothesize that static and dynamic feature sets will be able to diagnose MDD in different subsets of population. It is pertinent to utilize their full predictive capabilities in a combined model. In this experiment, whether a joint set of features from different sets can improve the accuracy was tested. Thus apart from using static and dynamic features separately, we tested all the possible combination of different feature sets. The feature combination was accomplished using concatenation of raw features selected from different feature sets using corresponding feature selection algorithms. The combined feature sets that performed better than previously best known accuracy are reported in the classification performance.

E. Classifier

Each set of the features described before employs either Support Vector Machine (SVM) or Random Forest (RF) classifiers to learn classifiers since these two classifiers have been demonstrated to work reasonably well for limited samples. Specifically SVM with radial basis function (RBF) and linear kernel was utilized for all the experiments. In case of SVM with RBF kernel, a standard set of parameters $\gamma \in \{0.1 \times 2^i | i = -10, -9.., 9, 10\}$ is followed using in-fold cross-validation. The hyper-parameter C for SVM learning algorithm is kept at 1, $i.e.$, $C = 1$. For RF, number of trees was chosen based on cross-validation by varying its range from 3 to 30.

All the classification results are shown in terms of leave-one-out test accuracy. During the leave-one-out classification process, training and testing process was run 82 times ($i.e.$, number of subjects). For each iteration, training was carried out on 81 subjects using SVM/ RF, and a test was performed on the left-out subject. The test accuracy was averaged across the 82 subjects to calculate the final accuracy values. Note that, all the feature selections were performed in-fold, $i.e.$, separate feature selection was done each time on the training set so that there was no possibility of information leakage. This process reduces the problem of overfitting for small sample sets. Apart from the leave-one-out classification accuracy, specificity and sensitivity were also calculated to validate our approach.

A pipeline demonstrating the whole experimental process is shown in Fig. 1.

III. Results

This section presents the classification results using the features described in Section II. Moreover, we also present the regions, edges and the predictive sub-network extracted through ranking based on *sub-graph* entropy.

A. Classification using Correlation Coefficients

From correlation coefficients, 10 values that are most significant based on minimum redundancy maximum relevance (mRMR) feature selection [40] were extracted using in-fold validation. Note that other feature selection algorithms such as MUSE could also be used [41]. The features are selected from frequency-band B2. Pearson's correlation values were able to classify MDD *vs.* healthy with an accuracy 0.74, specificity 0.64 and sensitivity 0.82 as shown in Table II using a leave-one-out classification method. The functional connectivity between FrontalPoleL - TemporalPoleR, PrecuneusL - RostralAntCingulateR and CerebCortL - BanksstsL were selected 82 out of 82 times during the mRMR feature selection and leave-one-out classification [25], [42], [43].

B. Classification using Network Features

1) Network Features: From brain network features, 10 most important integration and segregation features were extracted from network through in-fold mRMR feature selection. Network features had a leave-one-out classification accuracy of 0.67 with 0.84 sensitivity and 0.42 specificity (Table II). Among the features elected through this process, Clustering coefficient of insula (at sparsity 50%) and clustering coefficient of caudal middle frontal (at sparsity 50%) were selected in each fold by the mRMR feature selection process. Frequency sub-band B2 had highest classification performance in this set of features as well. Furthermore, a combination of feature values extracted from correlation and network analysis increased the accuracy to 0.79 with sensitivity 0.86 and specificity 0.70 as described in [25].

2) Node Entropy: For static *sub-graph* entropy based network analysis of MDD, we followed the same methodology described in our previous work [6] for diagnosing OCD from rs-fMRI. Node entropy was found to be most discriminating in the lower frequency band (B2). Differential node entropy was used to identify the neuronal units that are affected the most during MDD. These regions had the highest ranks when ranking of brain regions were performed using differential node entropy between MDD *vs.* healthy. The top-25 brain areas extracted through this process are listed along with their differential node entropy and p-values in Table S1 (SI). There were four regions that had statistically different node entropy values ($p \leq 0.05$) among the top ranked regions. However as expected, node entropy metric elevated the ranking of regions that are traditionally thought to be parts of default mode network [9] [44]. This network is active in awake-rest condition. When used as features for classification, node entropy of top-25 regions had the following leave-one-out classification performance: accuracy 0.67 with specificity 0.42 and sensitivity 0.84 (same as network features). The ranking is expected to elevate the regions from executive control circuitry, default mode network and salience network [45] as they have been traditionally hypothesized to be affected during adolescent MDD. The ranking process based on differential node entropy captured a number of

regions from these large-scale functional network among the highest 30% of all the regions in the atlas.

C. Extracting Predictive Sub-network

1) Accuracy of Predictive Sub-network: For edge entropy based network analysis of MDD, we followed the same methodology described in our previous work [6] for diagnosing OCD from rs-fMRI. Edge entropy was found to be most discriminating in the lower frequency band (B2). The edge ranking was performed 82 times, and in each iteration edges with most differential edge entropy were selected for leave-one-out classification. The number of edges chosen for classification was based on the performance over various number of edges. In Fig. S2 in Supplementary Information, we plotted the classification accuracies with changing the number of functional links in the predictive *sub-graph*. It is clear that 105 edges have the best leave-one-out prediction performance using SVM (RBF kernel). Similar to [6], the leave-one-out classification performance for MDD *vs.* healthy mimics the performance of a feature selection method. The classification accuracy increases until adding 105 edges but then the performance starts to degrade. The comparisons of classification results between the proposed predictive sub-network and other baseline techniques is shown in Table II.

When used as features, edge entropies of the extracted sub-network achieves 0.80 accuracy with identifying 25 out of all healthy and 41 out of 49 MDD subjects correctly. Although the edge ranking process in each group identifies the edges in the frontal, medial and the default mode network (DMN), the *differential edge entropy* promotes the edge that are traditionally though to be part of fronto-parietal, salience, executive and fronto-limbic network. Among them edges with most changes in *differential edge entropy* connect regions such as putamen, pallidum, thalamus, amygdala, caudate and accumbens.

2) Sub-network Visualization and Statistical Analysis: The predictive sub-network is illustrated in Fig. 3. This network comprises 33 regions and 105 edges. We have provided a table containing the top 25 regions from predictive sub-network in Table S1 in Supplementary Information. To demonstrate that the edges identified using *differential edge entropy* are stable across the group of subjects, we performed a leave-one-out test and plotted their occurrence in a histogram. Thus in each iteration, 105 high ranked edges were selected based on 80 subjects. Among these 105 regions, we calculated how many of them belong to the predictive network and plotted the frequencies Fig. S3 in Supplementary Information. This histogram in uniform and decays slowly signifying that the predictive edges are stable across the subjects in the group. Additionally we showed box-plots for *sub-graph* entropy values of the predictive sub-network for both healthy and MDD groups in Fig. 4. Here MDD subjects have lower entropy compared with healthy (with $p = 0.13$).

D. Dynamic Functional Connectivity:

Dynamic connectivity features extracted through tensor, ICA and PCA in isolation had a lackluster performance compared to static features. Constrained-PARAFAC with 20 components yielded an accuracy of 0.61 with sensitivity 0.96 and specificity 0.15, respectively. The classifiers were chosen based on the performance of SVM and random forest. The classification performance along with best performing classifiers are shown in Table II. ICA produced accuracy of 0.62 with sensitivity 0.92 and specificity 0.18, respectively, whereas the corresponding results for PCA were 0.57, 0.86 and 0.15. Random forest classifier (number of trees = 10) had the best performance while using ICA and PCA features. Notably, ICA had the best accuracy and specificity values among the dFC features. Constrained-PARAFAC had the best sensitivity.

E. Combined Feature Set from Static and Dynamic Connectivity:

From the static and dynamic connectivity measures as shown in Table II, the feature sets having the highest sensitivity and specificity were identified. Incidentally the feature set with highest specificity belonged to static features whereas the feature set with highest sensitivity belonged to dynamic features. We hypothesized that a combination of these feature sets will further improve the classification performance since static and dynamic feature sets may identify different subsets of the population. Thus edge entropies of predictive sub-network and constrained-PARAFAC were concatenated to create feature vectors for each subject as described in the Methods Section. A leave-one-out cross-validation using this combined feature improved the performance to accuracy of 0.82 (3% increase compared to individual feature sets), sensitivity of 0.84 and specificity of 0.79. The static and dynamic feature sets separately had overlap in correctly classifying 41 out of 82 subjects, whereas static predictive network features identified 16 subjects that were not identified correctly by constrained-PARAFAC. Also, constrained-PARAFAC identified 9 distinct subjects that were not identified correctly by the predictive network. This validates our hypothesis that static and dynamic feature sets can classify different subsets of patient $vs.$ healthy population more accurately. Additionally, six other combinations of features concatenation involving static and dynamic features were tested for completeness - edge entropy+correlation (115 features, accuracy 0.79), edge entropy+network (115 features, accuracy 0.80), edge entropy+correlation+network (125 features, accuracy 0.78), tensor+correlation+network (40 features, accuracy 0.65), tensor+correlation (30 features, accuracy 0.67) and tensor+network (30 features, accuracy 0.65). These feature concatenation processes did not improve the classification performance.

IV. Discussion

This paper explored the viability of automated diagnostic process for adolescent MDD patients based on rs-fMRI. We explored the feasibility of a combined static-dynamic feature combination scheme using edge entropy and tensor components for identifying a predictive sub-network and classification of adolescent MDD *vs.* healthy controls. The features that had the highest classification performance belonged to hemodynamic response frequency band B2 ($0.03 \sim 0.06$ Hz). This section discusses important observations from different classification schemes from the results mentioned in Section III.

A. Regions and Edges

Previous neuroimaging studies involving MDD patients have connected the dysfunction of fronto-limbic circuitry. This sub-network has traditionally been responsible for regulating human emotion. Literature support for the involvement of this sub-network in MDD can be found in [46]–[48]. Traditionally, regions such as amygdala, insula and prefrontal cortex were demonstrated to have differential functions for youths with MDD. In particular, an imbalance in synchronization between the frontal regions (responsible for controlling) and limbic areas specifically anterior cingulate cortex or ACC (responsible for emotion) [49] is thought to cause severe symptoms for MDD patients [50]. Neuroimaging studies have also implicated reduced functional connectivity between ACC and temporal-frontal brain regions [51]. Children with depression also showed atypical functional network connections in ACC and posterior cingulate cortex (PCC) [52], [53]. This was hypothesized to be associated with lower levels of emotion regulation capability among the participant children. Additionally, adolescent MDD duration was shown to associate with the connectivity between amygdala and post central gyrus [47].

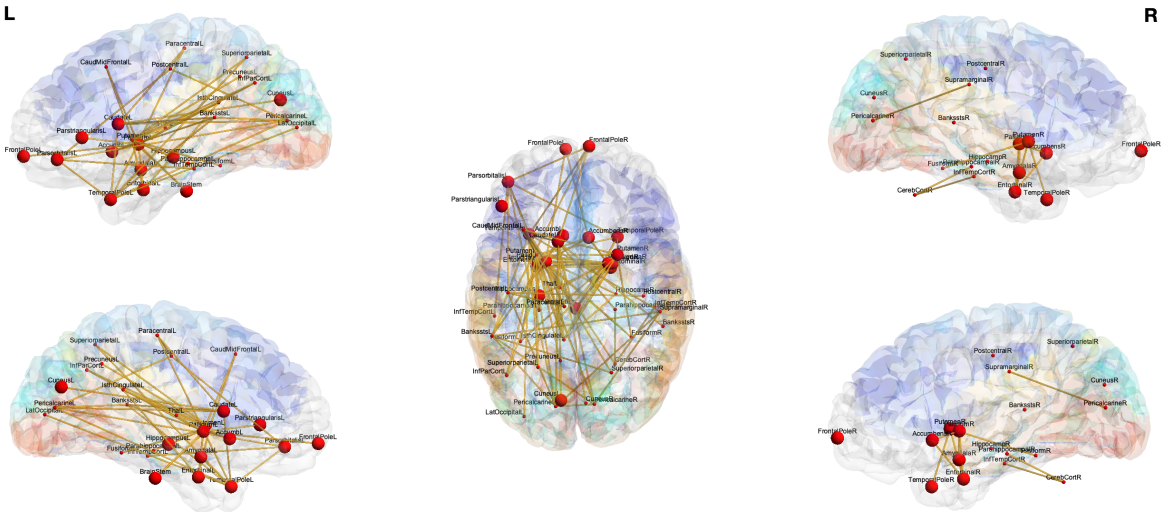

Fig. 3: Proposed predictive sub-network identified using *differential edge entropy*.

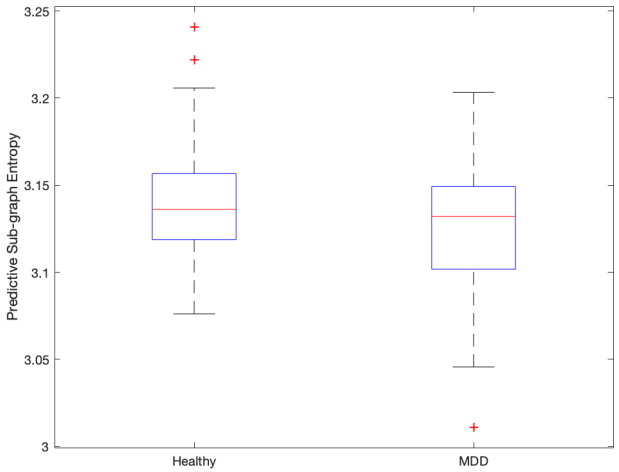

Fig. 4: Box-plot of *sub-graph entropy* values of the proposed predictive sub-network for MDD and healthy adolescent groups.

The proposed method and predictive sub-network are able to extract well-known default mode network regions for rs-fMRI scans from healthy humans [54]. For resting-state brain networks, all top regions extracted are either default mode or associated with resting-state. Adolescent MDD group showed higher differential node entropy for regions such as putamen, pallidum, accumbens, cingulate, postcentral gyrus, amygdala, pars-orbitalis and thalamus. Some of these regions were also identified in [6], [25] to have higher change in node entropy between healthy and disease states. These regions are part of the fronto-limbic circuit [55] in the brain.

Fig. 3 illustrates the sub-network that was extracted using the leave-one-out classification process for healthy *vs.* adolescent MDD. As can be seen in the brain plot, the network consists of a number of nodes that have more connections than the others and thus act as hub regions [33]. The edges include connections from frontal pole to striatal node. In case of MDD *vs.* healthy, the link between DMN and limbic system also has higher importance. Additionally the sub-network contains regions like accumbens, putamen, operculum, thalamus.

B. Dynamic Functional Connectivity

Dynamic connectivity approaches separately were not able to perform the classification task with higher accuracy. They had very high sensitivity, *i.e.*, they could identify true MDD subjects but had difficulty identifying the healthy controls. The poor specificity may be due to the fact that rs-fMRI may not contain many different dynamic states between healthy *vs.* adolescent MDD patients. A task based fMRI may be able to magnify the state differences between healthy controls and MDD patients.

C. Validation

In order to demonstrate that the combined *static-dynamic* features have better than chance statistical significance for classification, binomial tests were performed on the results [6], [7]. The proposed feature set had significantly more predictive performance ($p = 9.24 \times 10^{-9}$ for classifying healthy *vs.* adolescent MDD with respect to a naive random chance classifier. However, with respect to [34], the test yielded $p = 0.32$. A box-plot containing the *sub-graph* entropies for predictive network is illustrated in Fig. 4. It is evident that, MDD patients tend to have lower entropy compared to healthy controls. We have included the relationship between prediction probability of predictive sub-network + constrained-PARAFAC and CDRS in Fig. S4 (SI). Also we show the relationship between prediction probability and BDI in Fig. S5 (SI).

In fMRI literature, Fisher z-transformation is used to test hypotheses about the value of population correlation coefficient between two brain regions represented by nodes. The premise of our study is different; we are interested in classification of adolescent MDD patients from typically developing controls. We do not assume any underlying distribution of functional edge weights for the subjects to validate a hypothesis. Our predictive study looks for patterns in the functional connectivity based on static and dynamic features without any assumption of their distributions and thus Fisher z-transformation is not a necessity for calculating the features and training the classifiers.

D. Predictive Sub-network as Part of Other Known Networks

The key observations from our experiments implied that a number of regions and functional connections from brain sub-networks that were discovered before and well-known in fMRI literature are affected for adolescent MDD.

1) Default Mode Network (DMN): During rest, when a person is not actively doing a particular task, some regions of brain show increased activation. The network consisting these regions comprise the so called default mode network of human brain [9], [56]. These regions active during rest are thought be responsible for our day dreams, wandering minds, self ruminations etc. The algorithm prescribed in this paper using differential *sub-graph* entropy is able to extract regions such as cingulate cortex, temporal pole, parahippocampus, precuneus and medial prefrontal cortex, that are traditionally thought

to be part of DMN. Previous results have supported the hypothesis that the DMN is altered in adolescents with MDD [57], [58].

2) Salience: Salience network (SN) is comprised of regions that show increased activation when a person tries to decide where to focus their attention. Additionally, SN supports a mechanism that helps subjects attend important visual/other cues that are prominent compared with the background. The adolescent MDD predictive network includes entorhinal, hippocampus from SN [59], [60] network. Apart from that, salience network involves regions from cingulate, pallidum, thalamus etc. The regions and functional edges extracted through leave-one-out process may indicate that adolescent MDD subjects focus on physical cues in a different way compared to healthy adolescents [61], [62].

3) Executive Network: The executive network (EN) of human brain consists of neuronal units from frontal-parietal network. EN is hypothesized to support higher cognitive functions in humans, *e.g.*, making a decision and/or solving a problem at hand. Many nodes belonging to fronto-parietal network were extracted as part of the predictive sub-network (Fig. 2). These regions include parsorbitalis, hippocampus, caudate, frontal pole, temporal cortex, and putamen. The implication of these fronto-parietal regions may illuminate a possible change in executive network functions for adolescents suffering from MDD in comparison with healthy subjects [45], [63].

4) Fronto-Limbic: Fronto-limbic system in brain controls the resistance of distraction for any goal oriented behavior. The predictive sub-network consists of regions from this special brain circuits. Regions such as accumbens, hippocampus and postcentral in the predictive network are responsible for lower-level emotional responses in brain (fight or flight). Their dysfunction for adolescent MDD has been reported in the literature [45], [57].

V. Conclusion and Future Work

This paper explored a number of rs-fMRI based static and dynamic connectivity approaches to classify adolescents with MDD *vs.* healthy subjects. Using edge entropy and leave-one-out analysis, we showed that a predictive sub-network containing subsections of multiple large scale brain networks yields good prediction performance in terms of accuracy and specificity. The regions and edges in this sub-network indicate possible functional deterioration of brain circuits during adolescent MDD. However, features exploiting dynamic connectivity approaches alone did not yield good performance. Instead, the combined feature set from static and dynamic connectivity had the highest classification accuracy. Some of the regions and edges extracted by high differential *sub-graph* entropy had significantly different *sub-graph* entropy values. Potential limitations of the current model include small number of samples and non-availability of a hold out set. In the current work, classification step was done through past classification techniques. In image processing, the popular classifiers are Convolutional Neural Networks (CNNs) and Long-Short Term NNs which are innovative deep learning classifiers. Since we only have 82 samples, we refrained from describing deep learning models in the paper. However as the number of samples increases for adolescent MDD vs. healthy subjects, we plan to leverage the power of deep learning in future works. Combining features from different modalities, *e.g.*, diffusion MRI, fMRI and MEG should also be explored for the classification problem in the future. Additionally, efforts will be directed towards understanding effect of psychotropic medications on MDD patients with respect to *sub-graph* entropy and validating the proposed classification scheme for publicly available adult MDD datasets such as [64].

VI. Code Availability

The codes for graph entropy and dynamic connectivity are available at `https://github.com/parhi/SubgraphEntropy` and `https://github.com/parhi/TensordFC`, respectively.

References

[1] H. Ritchie and M. Roser, "Mental health," *Our World in Data*, 2019, https://ourworldindata.org/mental-health.

[2] K. Grabill, L. Merlo, D. Duke, K. L. Harford, M. L. Keeley, G. R. Geffken, and E. A. Storch, "Assessment of obsessive–compulsive disorder: a review," *Journal of Anxiety Disorders*, vol. 22, no. 1, pp. 1–17, 2008.

[3] A. S. Panayides, A. Amini, et al., "AI in medical imaging informatics: Current challenges and future directions," *IEEE Journal of Biomedical and Health Informatics*, vol. 24, no. 7, pp. 1837–1857, 2020.

[4] D. S Bassett, B. G. Nelson, B. A. Mueller, J. Camchong, and K. O. Lim, "Altered resting state complexity in schizophrenia," *Neuroimage*, vol. 59, no. 3, pp. 2196–2207, 2012.

[5] T. Xu, K. R. Cullen, B. Mueller, M. W. Schreiner, K. O. Lim, S. C. Schulz, and K. K. Parhi, "Network analysis of functional brain connectivity in borderline personality disorder using resting-state fMRI," *NeuroImage: Clinical*, vol. 11, pp. 302–315, 2016.

[6] B. Sen, G. A. Bernstein, B. A. Mueller, K. R. Cullen, and K. K. Parhi, "Sub-graph entropy based network approaches for classifying adolescent obsessive-compulsive disorder from resting-state functional MRI," *NeuroImage: Clinical*, vol. 26, pp. 102208, 2020.

[7] B. Sen, N. Borle, R. Greiner, and M. Brown, "A general prediction model for the detection of ADHD and autism using structural and functional MRI," *PloS One*, vol. 13, no. 4, 2018.

[8] B. Sen and K. K. Parhi, "Extraction of common task signals and spatial maps from group fmri using a parafac-based tensor decomposition technique," in *2017 IEEE International Conference on Acoustics, Speech and Signal Processing (ICASSP)*. IEEE, 2017, pp. 1113–1117.

[9] M. D. Greicius, B. Krasnow, A. L. Reiss, and V. Menon, "Functional connectivity in the resting brain: a network analysis of the default mode hypothesis," *Proceedings of the National Academy of Sciences*, vol. 100, no. 1, pp. 253–258, 2003.

[10] B. Sen, S.-H. Chu, and K. K. Parhi, "Ranking regions, edges and classifying tasks in functional brain graphs by sub-graph entropy," *Scientific Reports*, vol. 9, no. 1, pp. 7628, 2019.

[11] K. E. Joyce, P. J. Laurienti, J. H. Burdette, and S. Hayasaka, "A new measure of centrality for brain networks," *PLoS One*, vol. 5, no. 8, pp. e12200, 2010.

[12] V. Latora and M. Marchiori, "Efficient behavior of small-world networks," *Physical Review Letters*, vol. 87, no. 19, pp. 198701–1–4, 2001.

[13] O. Sporns, "Graph theory methods for the analysis of neural connectivity patterns," in *Neuroscience Databases*, pp. 171–185. Springer, 2003.

[14] M. Rubinov and O. Sporns, "Complex network measures of brain connectivity: uses and interpretations," *Neuroimage*, vol. 52, no. 3, pp. 1059–1069, 2010.

[15] L. C. Freeman, D. Roeder, and R. R. Mulholland, "Centrality in social networks: Ii. experimental results," *Social Networks*, vol. 2, no. 2, pp. 119–141, 1979.

[16] M. E. J. Newman, "Modularity and community structure in networks," *Proceedings of the National Academy of Sciences*, vol. 103, no. 23, pp. 8577–8582, 2006.

[17] G. Sabidussi, "The centrality index of a graph," *Psychometrika*, vol. 31, no. 4, pp. 581–603, 1966.

[18] K. D. Mackenzie, "The information theoretic entropy function as a total expected participation index for communication network experiments," *Psychometrika*, vol. 31, no. 2, pp. 249–254, 1966.

[19] J. Shetty and J. Adibi, "Discovering important nodes through graph entropy the case of enron email database," *Proceedings of the 3rd International Workshop on Link Discovery*, pp. 74–81, 2005.

[20] J. Huang, Q. Zhu, X. Hao, X. Shi, S. Gao, X. Xu, and D. Zhang, "Identifying resting-state multifrequency biomarkers via tree-guided group sparse learning for schizophrenia classification," *IEEE Journal of Biomedical and Health Informatics*, vol. 23, no. 1, pp. 342–350, 2018.

[21] R. Armañanzas, M. Iglesias, D. A. Morales, and L. Alonso-Nanclares, "Voxel-based diagnosis of Alzheimer's disease using classifier ensembles," *IEEE Journal of Biomedical and Health Informatics*, vol. 21, no. 3, pp. 778–784, 2016.

[22] A. Dragomir, A. G. Vrahatis, and A. Bezerianos, "A network-based perspective in alzheimer's disease: Current state and an integrative framework," *IEEE Journal of Biomedical and Health Informatics*, vol. 23, no. 1, pp. 14–25, 2018.

[23] C. C. Armstrong, T. D. Moody, J. D. Feusner, J. T. McCracken, S. Chang, J. G. Levitt, J. C. Piacentini, and J. O'Neill, "Graph-theoretical analysis of resting-state fMRI in pediatric obsessive–compulsive disorder," *Journal of Affective Disorders*, vol. 193, pp. 175–184, 2016.

[24] B. Sen and K. K. Parhi, "Predicting biological gender and intelligence from fMRI via dynamic functional connectivity," *IEEE Transactions on Biomedical Engineering*, doi: 10.1109/TBME.2020.3011363, 2020.

[25] B. Sen, B. Mueller, B. Klimes-Dougan, K. Cullen, and K. K. Parhi, "Classification of major depressive disorder from resting-state fMRI," in *2019 41st Annual International Conference of the IEEE Engineering in Medicine and Biology Society (EMBC)*. IEEE, 2019, pp. 3511–3514.

[26] E. O. Poznanski and H. B. Mokros, *Children's depression rating scale, revised (CDRS-R)*, Western Psychological Services Los Angeles, 1996.

[27] A. T. Beck, R. A. Steer, and G. K. Brown, "Beck depression inventory-II," *Psychological Corporation, San Antonio*, vol. 78, no. 2, pp. 490–498, 1996.

[28] K. R. Cullen, Melinda K. Westlund, et al., "Abnormal amygdala resting-state functional connectivity in adolescent depression," *JAMA Psychiatry*, vol. 71, no. 10, pp. 1138–1147, 2014.

[29] M. Jenkinson, C. F. Beckmann, T. E. J. Behrens, M. W. Woolrich, and S. M. Smith, "FSL," *Neuroimage*, vol. 62, no. 2, pp. 782–790, 2012.

[30] G. H. Glover, T.-Q. Li, and D. Ress, "Image-based method for retrospective correction of physiological motion effects in fmri: Retroicor," *Magnetic Resonance in Medicine: An Official Journal of the International Society for Magnetic Resonance in Medicine*, vol. 44, no. 1, pp. 162–167, 2000.

[31] B. Fischl, "Freesurfer," *NeuroImage*, vol. 62, no. 2, pp. 774–781, 2012.

[32] R. S. Desikan, F. Ségonne, et al., "An automated labeling system for subdividing the human cerebral cortex on mri scans into gyral based regions of interest," *Neuroimage*, vol. 31, no. 3, pp. 968–980, 2006.

[33] E. Bullmore and O. Sporns, "Complex brain networks: graph theoretical analysis of structural and functional systems.," *Nature Reviews Neuroscience*, vol. 10, no. 3, 2009.

[34] B. Sen, G. A. Bernstein, T. Xu, B. A. Mueller, M. W. Schreiner, K. R. Cullen, and K. K. Parhi, "Classification of obsessive-compulsive disorder from resting-state fMRI," *IEEE 38th Annual International Conference of the Engineering in Medicine and Biology Society (EMBC)*, pp. 3606–3609, 2016.

[35] J. Richiardi, S. Achard, H. Bunke, and D. Van De Ville, "Machine learning with brain graphs: Predictive modeling approaches for functional imaging in systems neuroscience," *IEEE Signal Processing Magazine*, vol. 30, no. 3, pp. 58–70, 2013.

[36] Y. Du, S. Fryer, et al., "Dynamic functional connectivity impairments in early schizophrenia and clinical high-risk for psychosis," *NeuroImage*, vol. 180, pp. 632–645, 2018.

[37] N. Leonardi, J. Richiardi, et al., "Principal components of functional connectivity: a new approach to study dynamic brain connectivity during rest," *NeuroImage*, vol. 83, pp. 937–950, 2013.

[38] M. J. Tobia, K. Hayashi, G. Ballard, I. Gotlib, and C. E. Waugh, "Dynamic functional connectivity and individual differences in emotions during social stress," *Human Brain Mapping*, vol. 38, no. 12, pp. 6185–6205, 2017.

[39] N. D. Sidiropoulos, L. De Lathauwer, X. Fu, K. Huang, E. E. Papalexakis, and C. Faloutsos, "Tensor decomposition for signal processing and machine learning," *IEEE Transactions on Signal Processing*, vol. 65, no. 13, pp. 3551–3582.

[40] H. Peng, F. Long, and C. Ding, "Feature selection based on mutual information: criteria of max-dependency, max-relevance, and min-redundancy," *IEEE Transactions on Pattern Analysis & Machine Intelligence*, , no. 8, pp. 1226–1238, 2005.

[41] Z. Zhang and K. K. Parhi, "MUSE: Minimum uncertainty and sample elimination based binary feature selection," *IEEE Transactions on Knowledge and Data Engineering*, vol. 31, no. 9, pp. 1750–1764, 2018.

[42] L. Schmaal, D.P. Hibar, et al., "Cortical abnormalities in adults and adolescents with major depression based on brain scans from 20 cohorts worldwide in the enigma major depressive disorder working group," *Molecular Psychiatry*, vol. 22, no. 6, pp. 900–909, 2017.

[43] W. C. Drevets, J. Savitz, and M. Trimble, "The subgenual anterior cingulate cortex in mood disorders," *CNS Spectrums*, vol. 13, no. 8, pp. 663–681, 2008.

[44] M. E. Raichle, A. M. MacLeod, A. Z. Snyder, W. J. Powers, D. A. Gusnard, and G. L. Shulman, "A default mode of brain function," *Proceedings of the National Academy of Sciences*, vol. 98, no. 2, pp. 676–682, 2001.

[45] C. Zhuo, G. Li, X. Lin, D. Jiang, Y. Xu, H. Tian, W. Wang, and X. Song, "The rise and fall of mri studies in major depressive disorder," *Translational Psychiatry*, vol. 9, no. 1, pp. 1–14, 2019.

[46] Q. Jiao, J. Ding, G. Lu, et al., "Increased activity imbalance in fronto-subcortical circuits in adolescents with major depression," *PloS One*, vol. 6, no. 9, 2011.

[47] C. Jin, C. Gao, C. Chen, S. Ma, R. Netra, Y. Wang, M. Zhang, and D. Li, "A preliminary study of the dysregulation of the resting networks in first-episode medication-naive adolescent depression," *Neuroscience Letters*, vol. 503, no. 2, pp. 105–109, 2011.

[48] K. Luking, G. Repovs, A. Belden, M. Gaffrey, K. Botteron, J. Luby, and D. Barch, "Functional connectivity of the amygdala in early-childhood-onset depression," *Journal of the American Academy of Child & Adolescent Psychiatry*, vol. 50, no. 10, pp. 1027–1041, 2011.

[49] W. C. Drevets, "Prefrontal cortical-amygdalar metabolism in major depression," *Annals of the New York Academy of Sciences*, vol. 877, no. 1, pp. 614–637, 1999.

[50] L. A. Hulvershorn, K. Cullen, and A. Anand, "Toward dysfunctional connectivity: a review of neuroimaging findings in pediatric major depressive disorder," *Brain Imaging and Behavior*, vol. 5, no. 4, pp. 307–328, 2011.

[51] K. R. Cullen, D. G. Gee, B. Klimes-Dougan, V. Gabbay, L. Hulvershorn, B. A. Mueller, J. Camchong, C. J. Bell, A. Houri, S. Kumra, et al., "A preliminary study of functional connectivity in comorbid adolescent depression," *Neuroscience Letters*, vol. 460, no. 3, pp. 227–231, 2009.

[52] M. Gaffrey, J. Luby, G. Repovš, A. Belden, K. Botteron, K. Luking, and D. Barch, "Subgenual cingulate connectivity in children with a history of preschool-depression," *Neuroreport*, vol. 21, no. 18, pp. 1182, 2010.

[53] M. Gaffrey, J. Luby, K. Botteron, G. Repovš, and D. Barch, "Default mode network connectivity in children with a history of preschool onset depression," *Journal of Child Psychology and Psychiatry*, vol. 53, no. 9, pp. 964–972, 2012.

[54] M. D. Greicius, K. Supekar, V. Menon, and R. F. Dougherty, "Resting-state functional connectivity reflects structural connectivity in the default mode network," *Cerebral Cortex*, vol. 19, no. 1, pp. 72–78, 2008.

[55] M. Oldehinkel, W. Francx, C. Beckmann, J. Buitelaar, and M. Mennes, "Resting state fmri research in child psychiatric disorders," *European Child & Adolescent Psychiatry*, vol. 22, no. 12, pp. 757–770, 2013.

[56] B. Biswal, F. Zerrin Yetkin, V. M. Haughton, and J. S. Hyde, "Functional connectivity in the motor cortex of resting human brain using echo-planar mri," *Magnetic resonance in medicine*, vol. 34, no. 4, pp. 537–541, 1995.

[57] G. S. Dichter, D. Gibbs, and M. J. Smoski, "A systematic review of relations between resting-state functional-mri and treatment response in major depressive disorder," *Journal of Affective Disorders*, vol. 172, pp. 8–17, 2015.

[58] T. Wise, L. Marwood, A. Perkins, A. Herane-Vives, R. Joules, D. J. Lythgoe, W. M. Luh, S. Williams, A. Young, A. Cleare, et al., "Instability of default mode network connectivity in major depression: a two-sample confirmation study," *Translational Psychiatry*, vol. 7, no. 4, pp. e1105–e1105, 2017.

[59] P. T. Bell and J. M. Shine, "Estimating large-scale network convergence in the human functional connectome," *Brain Connectivity*, vol. 5, no. 9, pp. 565–574, 2015.

[60] R. Yuan, X. Di, P. A. Taylor, S. Gohel, Y.-H. Tsai, and B. Biswal, "Functional topography of the thalamocortical system in human," *Brain Structure and Function*, vol. 221, no. 4, pp. 1971–1984, 2016.

[61] L. Hall, B. Klimes-Dougan, R. H. Hunt, K. M. Thomas, A. Houri, E. Noack, B. Mueller, K. Lim, and K. Cullen, "An fmri study of emotional face processing in adolescent major depression," *Journal of Affective Disorders*, vol. 168, pp. 44–50, 2014.

[62] R. H. Kaiser, J. R Andrews-Hanna, T. Wager, and D. A. Pizzagalli, "Large-scale network dysfunction in major depressive disorder: a meta-analysis of resting-state functional connectivity," *JAMA Psychiatry*, vol. 72, no. 6, pp. 603–611, 2015.

[63] H. Karim, C. Andreescu, D. Tudorascu, S. F. Smagula, M. A. Butters, J. F. Karp, C. Reynolds, and H. Aizenstein, "Intrinsic functional connectivity in late-life depression: trajectories over the course of pharmacotherapy in remitters and non-remitters," *Molecular Psychiatry*, vol. 22, no. 3, pp. 450–457, 2017.

[64] C. Yan, X. Chen, et al., "Reduced default mode network functional connectivity in patients with recurrent major depressive disorder," *Proceedings of the National Academy of Sciences*, vol. 116, no. 18, pp. 9078–9083, 2019.

Supplementary Information: Classification of Adolescent Major Depressive Disorder via Static and Dynamic Connectivity

Bhaskar Sen, *Student Member, IEEE*, Kathryn R. Cullen, and Keshab K. Parhi, *Fellow, IEEE*

S1: Sub-Graph Entropy

A. Node, Edge and Sub-Graph Entropy

An example of graph entropy and sub-graph entropy is shown in Fig. S1.

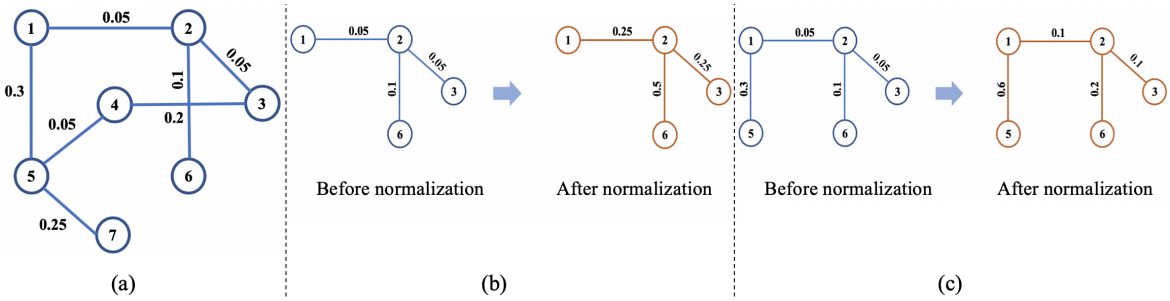

Fig. S1: a) An illustrative example of functional network among 7 nodes. The edges have been normalized, $i.e.$, they sum up to 1. *Graph entropy* of this network is $H(G) = -\sum_{i,j} q_{i,j} \log_2(q_{i,j}) = -[3 \times 0.05 \times \log_2(0.05) + 0.1 \times \log_2(0.1) + 0.2 \times \log_2(0.2) + 0.25 \times \log_2(0.25) + 0.3 \times \log_2(0.3)] = 2.466$ *bits*. b) Sub-network containing node 2 and its immediate neighborhood. The *node entropy* is 1.5 *bits*. c) Sub-network containing edge 1-2 and its immediate neighborhood. The *edge entropy* is 1.5709 *bits*.

S2: Illustrations

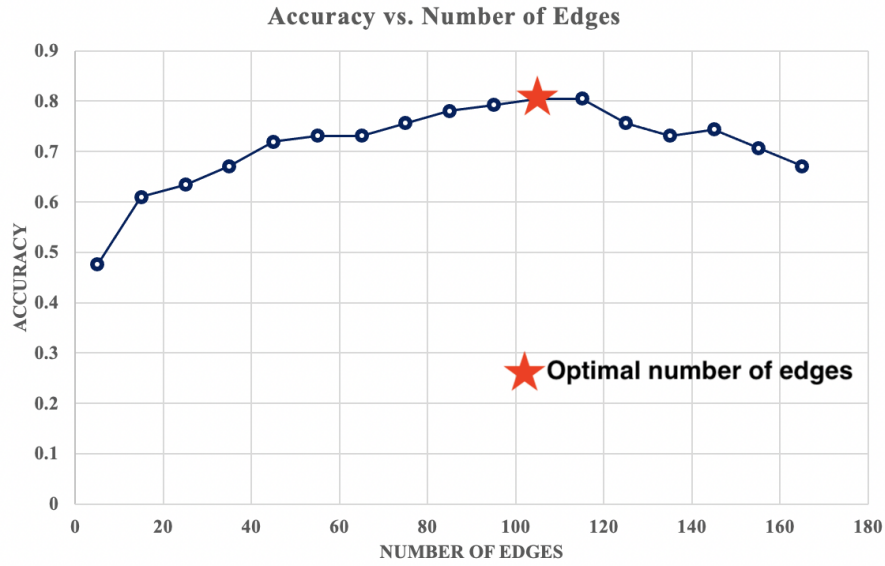

Fig. S2: Leave-one-out accuracy $vs.$ number of edges in sub-network.

Bhaskar Sen and Keshab K. Parhi are with Department of Electrical and Computer Engineering, University of Minnesota, Minneapolis (e-mail: parhi@umn.edu), Kathryn Cullen is with Department of Psychiatry and Behavioral Sciences, University of Minnesota, Minneapolis

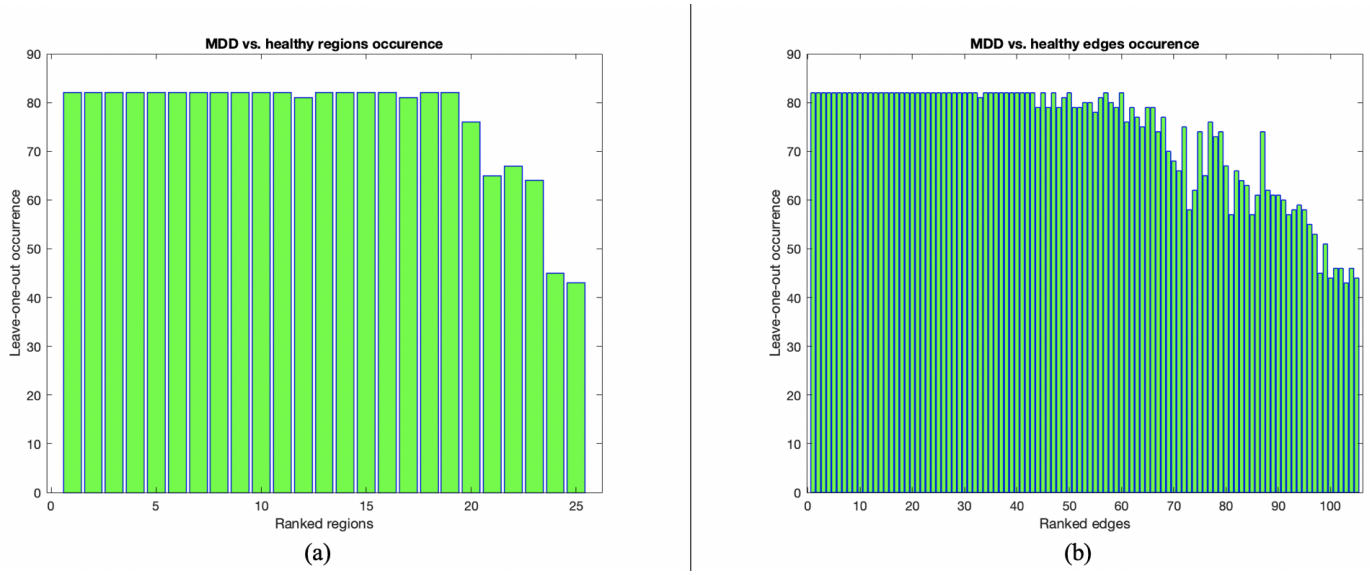

Fig. S3: Histogram of the edges and regions captured by leave-one-out training. X-axis represents edges/regions with corresponding rank.

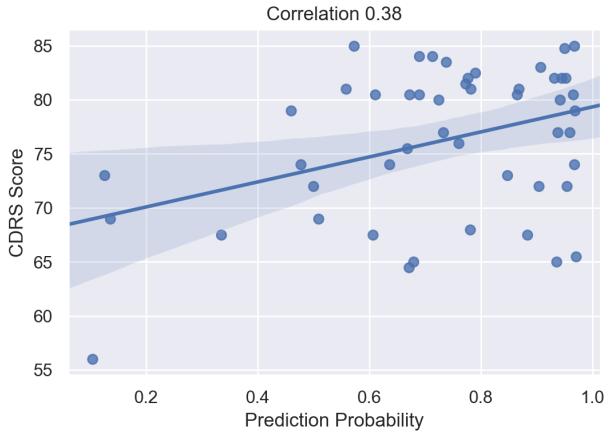

Fig. S4: Relationship between prediction probability of predictive sub-network + constrained-PARAFAC and Children's Depression Rating Scale (CDRS).

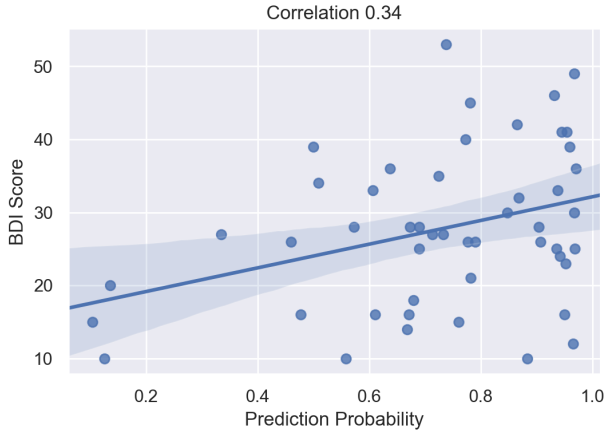

Fig. S5: Relationship between prediction probability of predictive sub-network + constrained-PARAFAC and Beck Depression Inventory (BDI).

S3: TABLES

TABLE S1: Top-25 highest ranked regions and their *differential node entropy* between adolescent MDD *vs.* healthy group.

Rank	Region / Hemisphere	Diff. Entropy	p-value
1	Putamen - L	0.5505	0.0076
2	Parsorbitalis - L	0.4662	0.0353
3	Pallidum - L	0.4126	0.1316
4	Putamen - R	0.4114	0.0477
5	Isthmus Cingulate - L	0.3796	0.0072
6	Accumbens - R	0.3509	0.1872
7	Entorhinal - R	0.3500	0.2403
8	Caudate - L	0.3280	0.1512
9	Pallidum - R	0.3134	0.2771
10	BrainStem	0.2890	0.3126
11	CerebCort - R	0.2881	0.2706
12	Pericalcarine - R	0.2792	0.1154
13	Pericalcarine - L	0.2694	0.1036
14	Postcentral - L	0.2682	0.1745
15	Supramarginal - R	0.2669	0.1727
16	Thalamus - L	0.2627	0.2208
17	Fusiform - R	0.2589	0.1316
18	Fusiform - L	0.2317	0.2052
19	Bankssts - L	0.2275	0.3956
20	CaudMidFrontal - L	0.2101	0.2655
21	Precuneus - L	0.2065	0.0946
22	Lateral Occipital - L	0.2005	0.3162
23	Bankssts - R	0.2003	0.3449
24	InfParCort - L	0.1959	0.2124
25	Amygdala - R	0.1898	0.4927

S4: ATLAS DETAILS

This section provides the details of the atlas regions and their corresponding coordinates in MNI152 space.

TABLE A1: Desikan Atlas Coordinates and Regions

X	Y	Z	Region
-22.43799052	-40.01410235	-49.10043329	Left_Cerebellum_Cortex
-9.365745637	2.239886304	-14.37367795	Left_Thalamus_Proper
-10.07260101	27.72348485	-12.26073232	Left_Caudate
-21.98422754	20.16952115	-20.84432891	Left_Putamen
-16.83028771	16.79043546	-23.15999222	Left_Pallidum
-0.075123916	-9.236922464	-48.42339352	Brain_Stem
-20.50547599	-2.062973884	-30.15532856	Left_Hippocampus
-19.81226823	15.48516687	-36.92135352	Left_Amygdala
-7.276182432	31.04307432	-27.10304054	Left_Accumbens_area
21.48534428	-39.86756307	-49.02782405	Right_Cerebellum_Cortex
9.483949985	2.061275227	-13.59662913	Right_Thalamus_Proper
11.78609914	26.20757004	-11.62715517	Right_Caudate
22.79048673	20.47876106	-20.71349558	Right_Putamen
17.75835396	15.67295792	-21.86726485	Right_Pallidum
22.00855593	-1.230696995	-31.1206177	Right_Hippocampus
20.08349546	15.711738	-37.17331388	Right_Amygdala
6.856174699	29.9811747	-26.78840361	Right_Accumbens_area
-46.56135363	-24.43048423	-8.671588408	ctx_lh_bankssts
-2.641475645	34.52602674	4.327244508	ctx_lh_caudalanteriorcingulate
-29.18799213	34.20815342	18.68062611	ctx_lh_caudalmiddlefrontal
-8.394193234	-59.99674691	0.810426155	ctx_lh_cuneus
-21.87644009	14.07402074	-47.78801843	ctx_lh_entorhinal
-30.9386489	-27.44044884	-34.66050092	ctx_lh_fusiform
-38.44759259	-46.19018519	10.055	ctx_lh_inferiorparietal
-45.16522307	-13.35528397	-36.35213969	ctx_lh_inferiortemporal
-6.797138047	-26.52777778	-0.606060606	ctx_lh_isthmuscingulate
-28.81817994	-68.91491475	-14.09027893	ctx_lh_lateraloccipital
-21.51043029	49.65374052	-35.04103453	ctx_lh_lateralorbitofrontal
-12.85870064	-50.95184803	-21.89164371	ctx_lh_lingual
-5.424302789	52.46314741	-33.96962151	ctx_lh_medialorbitofrontal
-51.38255075	-1.05607361	-29.19242037	ctx_lh_middletemporal
-20.70094021	-10.09763742	-33.50470106	ctx_lh_parahippocampal
-6.551643921	-8.080024814	28.71665633	ctx_lh_paracentral
-39.82481355	38.1677284	-3.969468614	ctx_lh_parsopercularis
-37.70623742	60.72183099	-31.45120724	ctx_lh_parsorbitalis
-41.22619629	47.33825684	-19.5916748	ctx_lh_parstriangularis
-11.2699553	-63.45146871	-10.27378672	ctx_lh_pericalcarine
-37.7076791	-0.500245339	17.57396958	ctx_lh_postcentral
-4.185311284	-0.283722438	12.20330739	ctx_lh_posteriorcingulate
-35.30378452	13.60621618	15.33101499	ctx_lh_precentral
-8.750484872	-38.07336113	13.38877036	ctx_lh_precuneus
-3.369775542	54.56656347	-17.64705882	ctx_lh_rostralanteriorcingulate
-27.43047381	65.73664656	-9.245512066	ctx_lh_rostralmiddlefrontal

X	Y	Z	Region
-8.409821118	46.32435307	13.8764545	ctx_lh_superiorfrontal
-21.121497	-41.68930512	23.69906348	ctx_lh_superiorparietal
-46.72014687	8.292424968	-21.74289591	ctx_lh_superiortemporal
-46.00677227	-13.25964187	10.55130854	ctx_lh_supramarginal
-5.798690205	78.87528474	-29.70529613	ctx_lh_frontalpole
-25.94376504	31.79330393	-52.99268244	ctx_lh_temporalpole
-36.91558442	-0.342938312	-11.6599026	ctx_lh_transversetemporal
-30.75487945	20.2217279	-20.08969575	ctx_lh_insula
48.03367217	-19.09704574	-10.55749682	ctx_rh_bankssts
5.245158888	35.7336147	3.08031281	ctx_rh_caudalanteriorcingulate
31.32239106	30.37378154	20.14012328	ctx_rh_caudalmiddlefrontal
5.413062284	-61.50735294	2.649221453	ctx_rh_cuneus
19.14095007	13.38072122	-47.39684466	ctx_rh_entorhinal
30.54333274	-25.02878436	-34.88151553	ctx_rh_fusiform
40.10512232	-41.90762888	9.178134557	ctx_rh_inferiorparietal
43.5415707	-8.394461078	-39.20629894	ctx_rh_inferiortemporal
5.855446927	-27.09696728	-1.528830806	ctx_rh_isthmuscingulate
28.27539489	-65.8775836	-18.00317174	ctx_rh_lateraloccipital
21.03270609	48.73015873	-34.47388633	ctx_rh_lateralorbitofrontal
9.887762593	-49.87773888	-19.71100632	ctx_rh_lingual
4.966974573	55.82042114	-33.24071315	ctx_rh_medialorbitofrontal
50.85591502	-4.637917276	-30.79573414	ctx_rh_middletemporal
21.59495927	-9.769602851	-33.93711813	ctx_rh_parahippocampal
5.574623858	-6.455534659	29.1560317	ctx_rh_paracentral
43.43193444	33.05039788	-5.577159909	ctx_rh_parsopercularis
39.84943842	55.80170411	-30.06438807	ctx_rh_parsorbitalis
44.60538203	44.68959732	-16.17094734	ctx_rh_parstriangularis
10.07145966	-62.11767266	-9.486723738	ctx_rh_pericalcarine
37.2218269	-2.29390681	18.21908602	ctx_rh_postcentral
4.539522514	1.299480455	13.94575705	ctx_rh_posteriorcingulate
35.74047669	11.18046754	17.23375229	ctx_rh_precentral
7.952909887	-39.13619703	12.41339621	ctx_rh_precuneus
5.23004886	53.77137622	-18.7896987	ctx_rh_rostralanteriorcingulate
29.98936817	63.1596294	-6.599787363	ctx_rh_rostralmiddlefrontal
10.21130626	44.56652488	15.72779455	ctx_rh_superiorfrontal
19.52022891	-44.67677003	23.1629292	ctx_rh_superiorparietal
47.22200315	10.34015441	-23.27712519	ctx_rh_superiortemporal
46.5050845	-10.93363136	9.673192179	ctx_rh_supramarginal
7.123893805	80.40376106	-25.63053097	ctx_rh_frontalpole
22.85859073	30.3030888	-51.48117761	ctx_rh_temporalpole
38.81806931	1.170792079	-13.0730198	ctx_rh_transversetemporal
32.27828362	19.71071121	-21.13080728	ctx_rh_insula